

APPLIED SCIENCES AND ENGINEERING

Determination of topographical radiation dose profiles using gel nanosensors

Karthik Pushpavanam¹, Sahil Inamdar¹, Subhadeep Dutta², Tomasz Bista³, Thaddeus Sokolowski³, Eric Boshoven⁴, Stephen Sapareto³, Kaushal Rege^{1*}

Despite the emergence of sophisticated technologies in treatment planning and administration, routine determination of delivered radiation doses remains a challenge due to limitations associated with conventional dosimeters. Here, we describe a gel-based nanosensor for the colorimetric detection and quantification of topographical radiation dose profiles in radiotherapy. Exposure to ionizing radiation results in the conversion of gold ions in the gel to gold nanoparticles, which render a visual change in color in the gel due to their plasmonic properties. The intensity of color formed in the gel was used as a quantitative reporter of ionizing radiation. The gel nanosensor was used to detect complex topographical dose patterns including those administered to an anthropomorphic phantom and live canine patients undergoing clinical radiotherapy. The ease of fabrication, operation, rapid readout, colorimetric detection, and relatively low cost illustrate the translational potential of this technology for topographical dose mapping in radiotherapy applications in the clinic.

INTRODUCTION

Radiation therapy is a mainstay of therapeutic options in cancer treatment, and development of new technologies has led to notable sophistication in the administration of radiotherapy. For example, multileaf collimation and state-of-the-art planning software permit the delivery of a higher conformal radiation dose to patients, which has led to improved outcomes and quality of life after treatment (1). In general, administration of radiotherapy necessitates the delivery of a high dose of radiation to the target tumor while minimizing dose delivered to the surrounding healthy tissue (2). Radiation doses prescribed to patients are dependent on both the nature and stage of the disease. Curative radiotherapy is typically delivered in fractions of small doses (fractionated radiotherapy) administered over multiple sessions, leading to a larger cumulative dose. Fractionated radiotherapy reduces the risk of long-term irreversible side effects, and typically, doses of ≈ 2 Gy are administered in a single session (3). However, in palliative radiotherapy, larger fractional doses are delivered (>3 Gy per treatment session) to conclude the treatment within a short span of time (3). However, various sources of error (4) including software errors in linear accelerators can lead to radiation overdosing and subsequent patient morbidity (5). Given the risk of accidental overexposure, independent verification of the radiation dose delivered at and near the target tissue can further advance patient safety (6).

Determination of topographical dose profiles along different tissues including oral cavity in head and neck and oral cancers; upper gastrointestinal (GI) tract in esophageal, head and neck, lung, and stomach cancers; and lower GI tract in colorectal, bladder, prostate, cervical, and bladder cancers can be critical in preventing overdosing of tissues and associated complications. Further, skin is the first organ exposed to external beam radiation and in cases of accidental exposure; overexposure of skin to radiation can lead to complications including erythema, desquamation, and necrosis (7). However, most clinically used sensors, including thermoluminescent dosimeters, ion chambers,

and silicon diodes, are capable of point dose measurements but are unable to map topographical radiation dose profiles, which obviate the identification of regions of overexposure (8). Radiographic films were developed to overcome these limitations and have been used to determine topographical dose information during radiotherapy. However, the post-irradiation wait time (typically >24 hours) required before dose prediction (9) and the inability to conform onto human anatomical features limit the routine clinical use of these films (10). In addition, performance of radiographic films is affected by operating conditions (e.g., humidity) that cause post-irradiation artifacts (11). There is a critical need for new technologies that can effectively report topographical dose distribution at or near tissues with minimal post-irradiation wait times for treatment planning, verification, and dosimetry.

Molecular and nanoscale sensors can overcome limitations with conventional systems and are practical alternatives as facile radiation sensors (12). Quantum dots and metal organic frameworks demonstrate an intense scintillating response but provide only point dose information limiting their application in the clinic (13, 14). Polymer gel dosimeters rely on sophisticated readout techniques [e.g., magnetic resonance imaging (MRI)] for post-irradiation analysis, which makes their clinical application cumbersome and expensive (15). Radiation-triggered conversion of a nonfluorescent monomer to a fluorescence-emitting polymer has been investigated for dose detection, but the response was susceptible to decay over time, potentially giving rise to challenges in measurement (16). In light of these limitations, there is a need to develop robust and facile sensors to qualitatively and quantitatively determine topographical (spatial) dose profiles in clinical radiotherapy.

Gold nanoparticles have unique physical and chemical characteristics that make them an excellent platform for the development of sensors (17–19). We recently developed a colorimetric sensor in which ionizing radiation engenders the formation of gold nanoparticles from its corresponding colorless salt precursors (20). Formulation of a gel-based nanosensor facilitates easier handling and application in clinical radiotherapy (21, 22). Here, we demonstrate the colorimetric visualization and quantification of spatial dose distribution profiles using a gel nanosensor. This approach combines the

Copyright © 2019
The Authors, some
rights reserved;
exclusive licensee
American Association
for the Advancement
of Science. No claim to
original U.S. Government
Works. Distributed
under a Creative
Commons Attribution
NonCommercial
License 4.0 (CC BY-NC).

¹Chemical Engineering, School for Engineering of Matter, Transport, and Energy, Arizona State University, Tempe, AZ 85287, USA. ²School of Molecular Sciences, Arizona State University, Tempe, AZ 85287, USA. ³Banner MD Anderson Cancer Center, Gilbert, AZ 85234, USA. ⁴Arizona Veterinary Oncology, Gilbert, AZ 85233, USA. *Corresponding author. Email: rege@asu.edu

ease of colorimetric detection with a rapid and robust response and facilitates the topographical mapping of radiation doses along tissue surfaces. We further demonstrate preclinical evaluation of the gel nanosensor technology for determining topographical dose distribution in live canine patients undergoing radiotherapy. Together, our results demonstrate the potential for clinical translation of the topographical dose determination technology using gel nanosensors for treatment planning and dose verification in cancer radiotherapy for human patients.

RESULTS

Accidental exposure of tissues to high levels of radiation during radiotherapy necessitates new technologies that can facilitate independent verification and visualization of the delivered dose over areas of the body that are at risk of exposure. However, there are no built-in dosimeters in cancer radiotherapy systems, and existing dosimeters lack the ability to report topographical dose distribution along tissue surfaces. Facile radiation sensors that are robust, predictive, easy to operate, and cost effective can lead to the development of new wearable instruments and detectors that can enable clinicians to effectively deliver radiation to target tissues, leading to increased safety and improved patient outcomes.

Here, we describe the development of a gel nanosensor technology for the visualization of topographical dose profiles of ionizing radiation (e.g., x-rays). The premise behind the topographical dose visualization technology is based on the conversion of gold ions to nanoparticles, which is accompanied by the development of a maroon color, only in the irradiated region of the gel nanosensor. In general, gold ions exist in a trivalent state (AuCl_4^-), which is first reduced to a metastable +1 valence state (AuBr_2^-) via a room temperature reaction with ascorbic acid (vitamin C) (23). Irradiation of gels with therapeutic levels of radiation leads to splitting of water molecules (radiolysis) into highly reactive free radicals including hydrated electrons, hydrogen free radicals, and hydroxyl free radicals (24). These radiolysis-generated hydrated electrons reduce the monovalent gold to its zerovalent state, leading to the formation of gold atoms, which nucleate and mature into gold nanoparticles. The formation of gold nanoparticles renders a maroon color to the originally colorless gel. The intensity of the maroon color varies with the radiation dose, and the range of linear response is used for calibrating the gel nanosensor. Addition of a quenching agent (sodium sulfide or Na_2S) restricts nanoparticle formation only to the irradiated regions of the gel, which facilitates topographical dose mapping.

We first determined the response of the fully irradiated gel to establish a calibration of absorbance with radiation dose (Fig. 1). All surfactant concentrations used in the study between 24.5 and 49 mM resulted in the formation of maroon-colored hydrogels upon exposure to ionizing radiation; the nonirradiated control remained colorless and translucent. The change in color was visibly observable to the naked eye within 10 min of exposure. We also observed an increase in the intensity of the gel nanosensor color with decreasing surfactant concentration for a fixed radiation dose. However, at the highest surfactant concentration (73.5 mM) used in the study, no visible color change was observed even after 30 min. We summarize these phenomena using illustrations for low and high concentrations of the surfactant (fig. S1). Hydrogen tetrachloroaurate dissociates into positively charged hydrogen ions (H^+) and negatively charged tetrachloroaurate ions (AuCl_4^-) in an aqueous solution (25). AuCl_4^-

(Au^{3+}) will likely complex with the permanently positively charged C_{14}TAB ($\text{CTA}^+ + \text{Br}^-$), leading to the formation of AuBr_4^- (25). Upon addition of ascorbic acid, AuBr_4^- is reduced by a two-electron transfer to AuBr_2^- (i.e., Au^{1+}) (25). At all concentrations of C_{14}TAB used in the study (24.5 to 73.5 mM), the surfactant exists in the form of micelles [critical micelle concentration (CMC) \approx 5 mM] (26). We reason that, at any given time, there are three distinct species, (i) free gold ions, (ii) C_{14}TAB micelles, and (iii) gold ions bound to C_{14}TAB micelles, and that there exists an equilibrium between them (27). At low surfactant concentrations, some Au^{1+} are free in solution and others are electrostatically bound to the micelles (28). With increasing surfactant concentration, there is an increase in the number of C_{14}TAB micelles in the system that further increases gold ion-bound C_{14}TAB micelles (27). Consequently, the number of free Au^{1+} decreases with a simultaneous increase in the gold-micelle complex. We posit that radiolysis leads to the reduction of only free Au^{1+} ions, ultimately leading to nanoparticle formation. We reason that this likely leads to a higher yield of nanoparticles at low surfactant concentrations due to the reduction of a higher number of free Au^{1+} ions to Au^0 when compared to the system at high surfactant concentration. These Au^0 atoms mature into gold nanoparticles through surface-assisted reduction of unreacted free Au^{1+} ions (29).

Following irradiation, a quantitative correlation between the intensity of the color formed in the gels and the delivered dose was determined using absorbance spectroscopy (Fig. 1, B to F). Radiation resulted in the formation of quasi-spherical gold nanoparticles that exhibited a characteristic light absorption spectral peak between 500 and 600 nm (17). A decrease in the width of the spectral profile is observed with increasing radiation dose, indicating a decrease in polydispersity of the nanoparticles formed. A blue shift in the absorbance peaks with increasing radiation dose suggests a decrease in particle size compared to those obtained at lower radiation doses (20). The peak absorbance intensity increases with increasing radiation dose, corroborating the observed increase in color intensity. A decrease in the peak absorbance at 540 nm was observed with increase in concentration of the cationic surfactant, likely due to micellar inhibition of the reduction of Au^{1+} to Au^0 (28), consistent with previous observations (20–22). The maximum peak absorbance at 540 nm was plotted as a function of the delivered radiation dose to quantify the gel nanosensor response (fig. S2). In general, the gel nanosensor was able to distinguish between incremental doses of radiation doses in a statistically significant manner (fig. S2), although this resolution is lost at the highest surfactant concentration (i.e., 73.5 mM).

We next determined the ability of the gel nanosensor to detect topographical distribution of the radiation dose by irradiating one-half of the gel nanosensor with a 4-Gy dose. The near-immediate (\approx 10 min) visual appearance of maroon color only in the irradiated region indicates the formation of gold nanoparticles in this area (Fig. 2). However, the color was observed to “bleed over” to the nonirradiated region 1 hour after exposure (Fig. 2A), which indicated a loss of topographical information in the gel over time. Increasing the weight percent of agarose from 1.5 to 2%, used to decrease the pore size in the gel (30), did not help preserve topographical integrity of dose distribution (Fig. 2B), indicating that the bleed-over phenomenon is not significantly influenced by gold nanoparticle diffusion but is likely a reaction-controlled phenomenon.

As an approach to maintaining topographical information of the delivered dose, we hypothesized that radiolytically generated gold nanoparticles act as seeds for unreacted gold ions on the nonirradiated

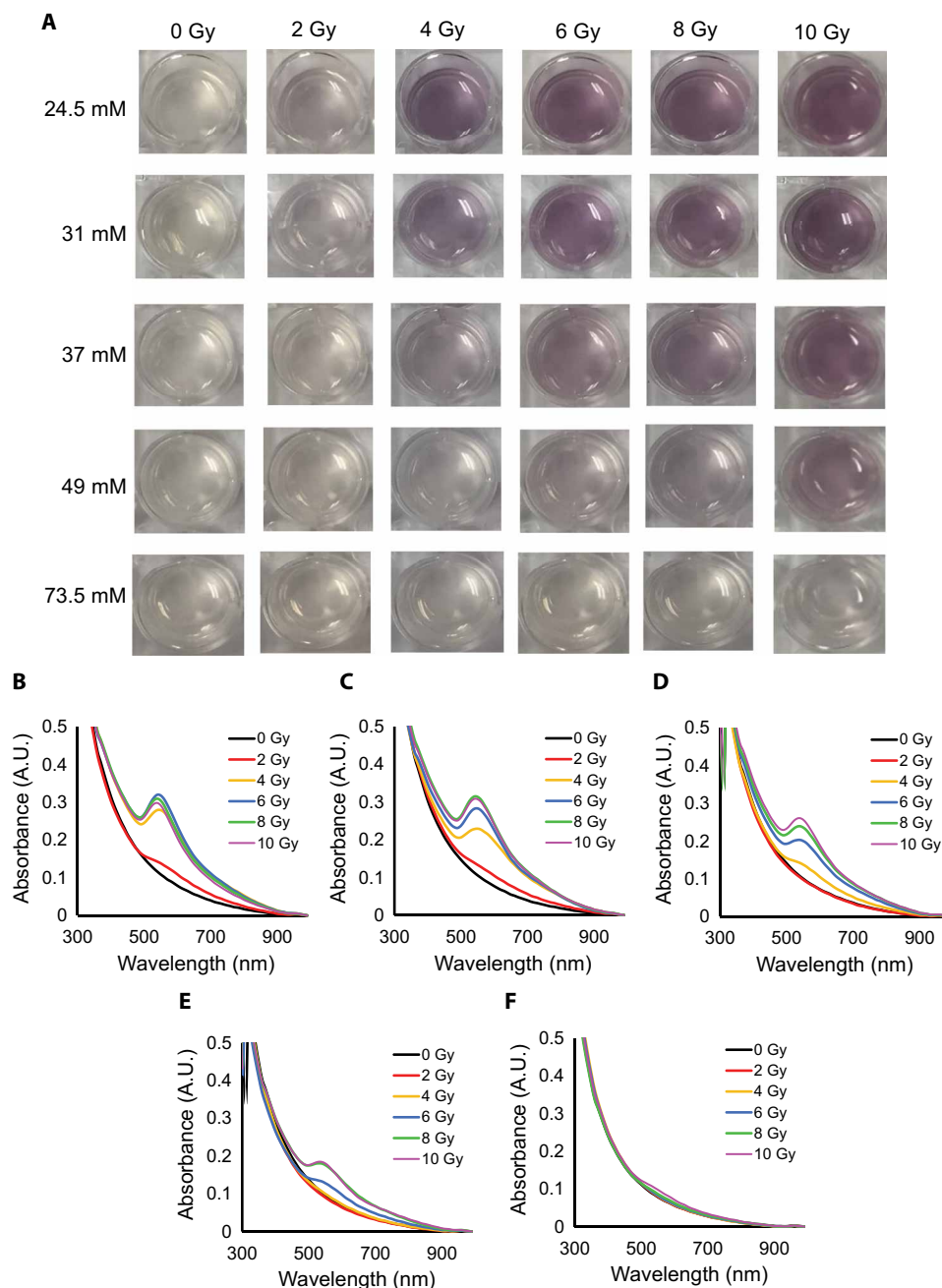


Fig. 1. Digital images and UV-visible spectra of different gel nanosensor formulations exposed to therapeutic doses of x-rays. (A) Images of gel nanosensors fabricated in 24-well cell culture plates and containing different concentrations of $C_{14}TAB$ (24.5 to 73.5 mM) upon exposure to various doses of ionizing radiation (0- to 10-Gy x-rays); Na_2S wait time was 5 min after irradiation, and incubation time was 10 min. Images were acquired 1 hour after irradiation. A visible increase in intensity in the maroon color is observed with increasing doses of ionizing radiation for most $C_{14}TAB$ concentrations used. (B to F) Absorbance spectra (300 to 990 nm) of the same gel nanosensors containing (B) 24.5 mM, (C) 31 mM, (D) 37 mM, (E) 49 mM, and (F) 73.5 mM irradiated using different radiation doses. Characteristic absorbance peaks between 500- and 600-nm wavelengths are indicative of gold nanoparticles formed in the gels. The corresponding radiation doses are mentioned in the legend with increasing radiation dose (top to bottom). A.U., arbitrary units. Photo credit: Sahil Inamdar, Arizona State University.

region, leading to the formation of additional gold nanoparticles (31). These additional gold nanoparticles, in turn, impart color to non-irradiated regions and drive the bleed-over phenomena, which lead to loss of topographical dose information. Incubation with sodium sulfide (Na_2S) for 10 min (10-min post-irradiation wait time before adding Na_2S) led to complete suppression of the color bleed over

(Fig. 2C); at similar concentrations, sodium halides (NaX , $X = Cl, Br, I$), however, were ineffective for this purpose. In the absence of sodium sulfide, growth of gold nanoparticles is thought to proceed via two distinct steps (29). The first step involves the reduction of Au^{1+} to Au^0 atoms, which nucleate and develop into small nanoclusters. The second step involves the growth and maturation of nanoparticles

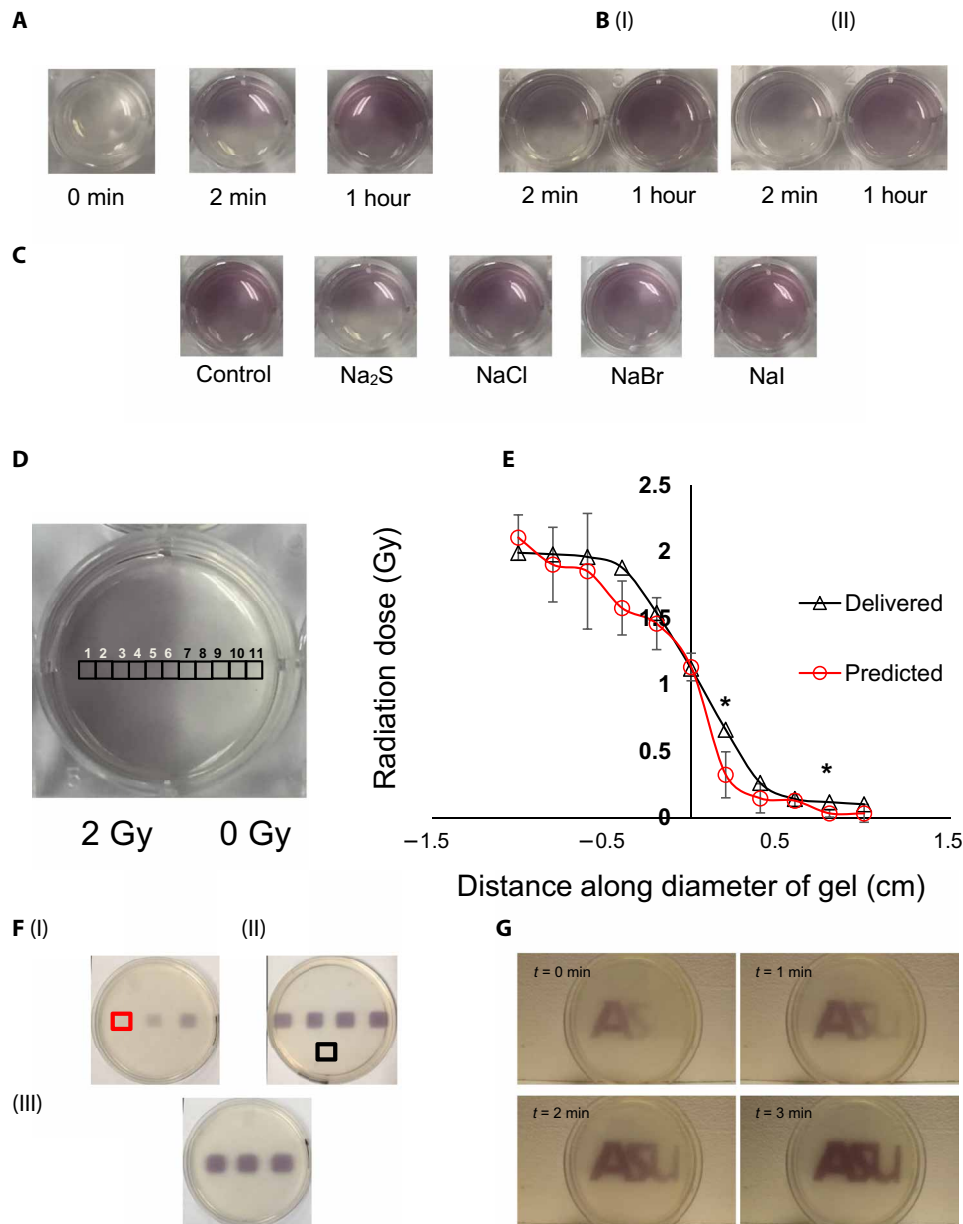


Fig. 2. Topographical visualization and quantification of radiation doses using gel nanosensors. (A) Gel nanosensor (left) before irradiation, (middle) top half irradiated with 4 Gy and image acquired 2 min after irradiation, and (right) image acquired 1 hour after irradiation. A visible increase in color intensity in the nonirradiated lower half indicates bleed over of color and loss of topographical information. (B) I: 1.5% (w/v) agarose gel (left) 2 min after irradiation and (right) 1 hour after irradiation; II: 2% (w/v) agarose gel (left) 2 min after irradiation and (right) 1 hour after irradiation indicates that the increase in agarose weight percentage does not preserve topographical dose information. (C) Gel nanosensor incubated with 5 mM sodium sulfide (Na₂S) and various sodium halides with a wait time of 10 min and incubation time of 10 min; images were acquired after 1 hour. No loss of topographical information is observed upon incubation with sodium sulfide. All gels were fabricated in 24-well plates. (D) Colorimetric response of the gel nanosensor irradiated on one-half with a 2-Gy x-ray dose. A visible appearance of maroon color in the irradiated region illustrates the ability of the gel nanosensor to visualize topographical dose profiles. Each black square box (labeled 1 to 11) on the gel nanosensor corresponds to a grid of size $\approx 2 \times 2$ mm, whose absorbance at 540 nm is determined. Grids starting from 1 to 5 are regions exposed to ionizing radiation, 6 is the grid at the edge of the irradiation field, and grids from 7 to 11 are regions outside the field of irradiation. (E) Dose fall-off profile for the gel nanosensor irradiated by 2 Gy on one-half. The delivered and predicted radiation doses are comparable, which indicates the efficacy of the gel nanosensor in visualizing and retaining topographical information. In all cases, Na₂S was added for 10-min incubation time after a wait time of 30 min. Radiation doses predicted by the gel nanosensor as compared with the delivered radiation dose as obtained from the treatment planning system. Asterisks indicate statistically significant differences ($P < 0.05$) between the delivered dose and the dose predicted by the gel nanosensor ($n = 3$ independent experiments). (F) Representative image of a petri dish containing the gel nanosensor formulation (≈ 3 mm thick and ≈ 10 cm diameter) irradiated with a 1 cm \times 1 cm square field of x-ray radiation. From the left, each square indicates increasing radiation dose from (I) 0.5 Gy (red box), 1 Gy, and 1.5 Gy; (II) 2, 2.5, 3, and 3.5 Gy; and (III) 4, 4.5, and 5 Gy; the black box in image (II) shows 0 Gy. (G) Visualization of a complex topographical dose pattern (ASU letters) generated using a 2-Gy x-ray dose. The petri dish has a diameter of ≈ 10 cm. In (F) and (G), the gel nanosensors contain 24.5 mM C₁₄TAB, and Na₂S was added after a wait time of 30 min and incubation time of 10 min; a representative image from three independent experiments is shown. Photo credit: Sahil Inamdar, Arizona State University.

due to binding and reduction of free gold ions onto existing nanoclusters and determines the overall size and the number of particles formed. We reason that quenching of the unreacted gold ions in the nonirradiated region is a critical step in preserving topographical dose information. Therefore, addition of sodium sulfide, which reduces the unreacted free gold ions to gold sulfide nanoparticles (32), inhibits the bleed-over phenomena and retains topographical dose information required for dose visualization and dosimetry.

The efficacy of the sodium sulfide treatment for preserving topographical dose information was investigated by optimizing the “wait time,” which is the duration between the completion of irradiation and addition of Na_2S , and the “incubation time,” which is the duration for which the Na_2S is incubated on the gel nanosensor. In all cases, the visual response was monitored and the corresponding quantitative correlation between the intensity of the color formed in the gels and the delivered dose was determined using absorbance spectroscopy (figs. S3 and S4). Increasing the wait time (fixed incubation time of 10 min) generally led to an increase in absorbance for a fixed radiation dose (fig. S5). For example, the average absorbance increased from 0.05 to 0.18 upon increasing the wait time from 2 to 30 min for the 6-Gy dose. Addition of Na_2S immediately (i.e., 2 min wait time) likely leads to the reduction of unreacted gold ions to gold sulfide particles. This can reduce the growth of radiolytically generated gold nanoparticles, which, in turn, is reflected in the lower absorbance values observed for the shorter wait times (fig. S5). Addition of Na_2S following longer wait times, 20 and 30 min, did not result in significant increase in the peak absorbance at 540 nm for all except one irradiation condition (2 Gy). It is likely that most of the radiation-generated nanoparticles mature at the longer wait times, and further addition of the quenching agent does not affect their final yield (fig. S6). Although the 20-min wait time was sufficient for saturating the gel nanosensor response, we used a 30-min wait time for all subsequent studies to ensure complete maturation of the radiation-generated gold nanoparticles. The gel nanosensor was formulated to detect doses delivered in conventional fractionated radiotherapy (i.e., 1 to 2 Gy per fraction). However, the sensor can be adopted for wider dose ranges used in modern radiotherapy by fine-tuning the concentration of the cationic surfactant and/or modulating the time of addition of sodium sulfide. This level of flexibility is not available in existing dose detection systems, which typically have a fixed linear response.

Studies on the effect of precursor gold salt concentration on gel nanosensor response indicated that for the same radiation dose, 0.25 mM HAuCl_4 exhibited a higher absorbance value at 540 nm when compared to 0.025 and 0.12 mM HAuCl_4 (fig. S7A). Higher precursor gold salt concentrations (0.12 and 0.25 mM) showed a significant increase in the yield of nanoparticles for doses between 0 and 4 Gy; this behavior was not seen at the lowest gold salt concentration investigated (0.025 mM; fig. S7, B and C). The percentage conversion of gold ions to nanoparticles in the system ranged from 2 to 13% under these conditions (fig. S7D). In general, the percent conversion increased with dose and remained largely invariant for >6-Gy doses.

Clinical radiotherapy for skin and breast cancer lesions commonly uses radiation field sizes that are larger than 3 cm × 3 cm in area (33–35). To accommodate larger radiation fields, we fabricated a gel nanosensor with the same thickness (≈ 3 mm) but with a larger diameter (≈ 3.5 cm). These gel nanosensors, containing 37 mM C_{14}TAB , were irradiated over the whole area, with doses ranging from 0 to 4 Gy, and treated with 5 mM Na_2S with a wait time of 30 min after irradiation (fig. S8A). Following irradiation, peak absorbances

at 540 nm of the irradiated and nonirradiated gel nanosensors were plotted as a function of radiation dose to obtain a linear calibration curve between 0 and 4 Gy (fig. S8, B and C). The predictive efficacy of the sensor was determined using a dose of 1.5 Gy, which was not used for generating the calibration curve. The change in color was quantified using the previously generated calibration curve, and the dose was estimated to be 1.28 ± 0.1 Gy, which is comparable to the delivered dose indicating the predictive ability of the gel nanosensor.

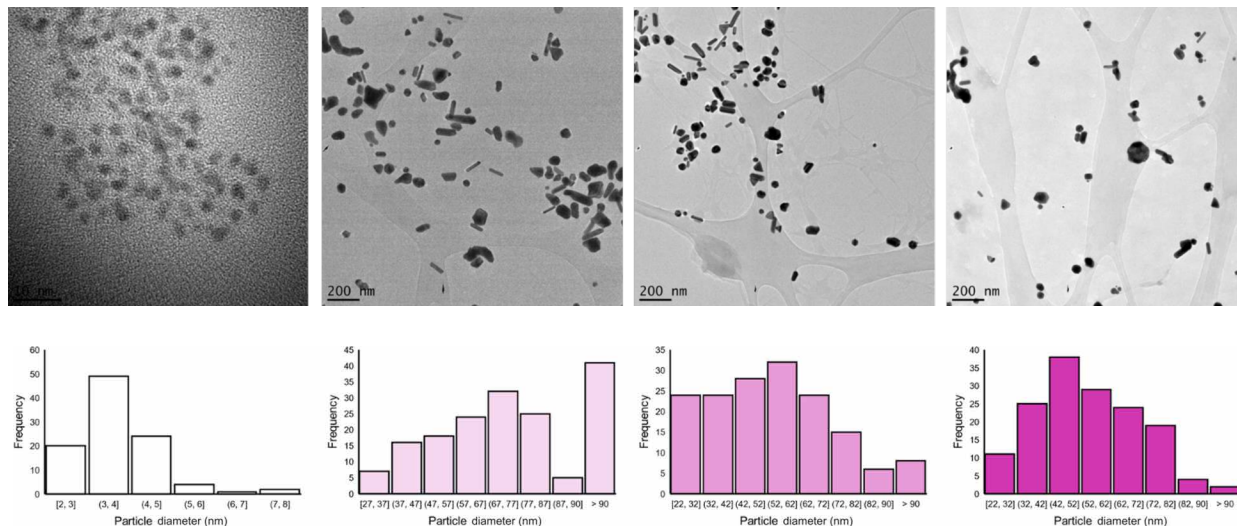
To investigate the ability to detect and quantify topographical dose distribution, one-half of the gel was irradiated with 2 Gy by positioning it at the edge of the radiation field and the other half was not irradiated (Fig. 2D). The absorbance at 540 nm was recorded in finite grids ($\approx 2 \times 2$ mm) along the diameter of the gel nanosensor, and the radiation dose was predicted using the previously established calibration curve. The topographical radiation dose profile predicted by the gel nanosensor is in excellent agreement with the delivered dose profile (Fig. 2E). In general, there were minimal statistical differences between the delivered dose and that predicted by the gel nanosensor under corresponding conditions. These results indicate the potential of the gel nanosensor for qualitatively and quantitatively detecting regions irradiated with ionizing radiation and distinguishing them from those that are not irradiated.

We further investigated the capability of the gel nanosensor for visualizing diverse topographical radiation dose patterns. The gel nanosensor was irradiated with a square field (1 cm × 1 cm) of x-rays with a 1-cm nonirradiated spacing between each field. Each sequential square was irradiated with incremental doses, resulting in multiple squares within the gel nanosensor. The increase in intensity of the color is indicative of the increasing dose while preserving the topographical integrity. Regions that are not irradiated do not demonstrate a change in color (Fig. 2F). These results also indicate a facile method for nanoparticle patterning in gels using radiation. We also demonstrated the capability of the gel nanosensor for detecting complex radiation patterns as shown by a model dose pattern that read “ASU” (Fig. 2G). In these studies, the radiation dose was delivered sequentially, which results in delayed appearance of the last two letters, viz. “S” and “U” compared to appearance of “A.”

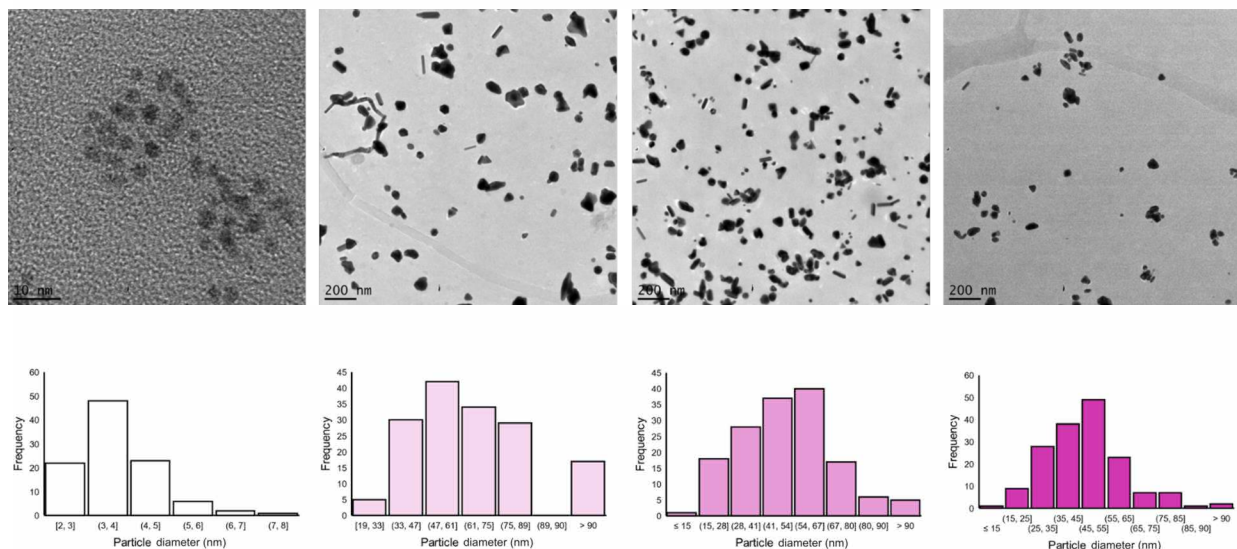
Transmission electron microscopy (TEM) analyses were carried out to characterize the size distribution of gold nanoparticles generated as a function of dose (Fig. 3). A reduction in the average nanoparticle diameter and polydispersity was observed at higher radiation doses (e.g., 6 Gy) when compared to the lower doses (e.g., 2 Gy) independent of the C_{14}TAB concentration used (24.5 and 37 mM). Energy-dispersive x-ray spectroscopy, used for elemental analysis, indicated two overlapping peaks in the nonirradiated region: (i) M-shell peak at 2.12 keV corresponding to gold and (ii) K-shell peak at 2.3 keV likely due to the presence of sulfur (fig. S9) (36). The irradiated region contained a higher yield of gold nanoparticles and displayed a sharp peak corresponding to only the M-shell of gold (fig. S9B). Comparison of both spectra indicates the formation of gold sulfide nanoparticles in the presence of Na_2S in the nonirradiated region. The absence/minimal presence of the sulfur peak in the irradiated region corroborated with the maroon color and an absorbance peak between 500- and 600-nm wavelengths, which is characteristic of gold nanoparticles formed in the gel nanosensor.

At high temperatures (e.g., $>90^\circ\text{C}$) in solution, agarose molecules adopt a random coil structure but, upon cooling ($<37^\circ\text{C}$), form a hydrogel, which contains helical bundles that are held together by

A



B



C

C₁₄TAB concentration	0 Gy	2 Gy	4 Gy	6 Gy
24.5 mM	4.0 ± 1.0 nm	64.4 ± 21.1 nm	51.6 ± 19.4 nm	47.0 ± 15.7 nm
37 mM	3.6 ± 0.9 nm	75.0 ± 26.1 nm	54.0 ± 18.8 nm	54.9 ± 17.7 nm

Fig. 3. Radiation-induced gold nanoparticle formation visualized and quantified using TEM images. TEM images showing the formation of nanoparticles for two different surfactant concentrations of (A) 37 mM and (B) 24.5 mM with a gold salt concentration of 0.25 mM after exposure to various levels of ionizing radiation. Na₂S was added after a wait time of 30 min in all cases and incubated for 10 min. Histograms of particle size distribution (diameter), determined using analysis of TEM images, are shown below each corresponding micrograph; quasi-spherical geometry was assumed for the nanoparticles. The histograms show distribution for a range of nanoparticle size (e.g., distribution between 39 and 49 nm is indicated as 39, 49, and so on). (C) Table showing average nanoparticle size (nm) ± 1 SD about the mean as a function of radiation dose for the two surfactant concentrations 24.5 and 37 mM.

hydrogen bonds (37). The resulting hydrogel contains pores whose heterogeneity and size decrease with increasing weight percent of the biopolymer (30, 38). Radiation-induced gold nanoparticle formation was therefore studied using four different weight percentages of agarose, 0.4, 0.75, 1.0, and 1.25%, and the change in the color formed following irradiation with 0, 2, 4, or 6 Gy was quantified using ultraviolet (UV)–visible spectroscopy (fig. S10). A broader absorbance peak was observed for the 0.4% agarose when compared to the 1.25% agarose, which indicates higher nanoparticle heterogeneity likely due to larger pore size and/or heterogeneity in case of the former gel. Area under the peak between 500 and 600 nm, used as an indicator of heterogeneity of the nanoparticle population, indicated lower heterogeneity in gels generated using higher weight percentages of agarose (fig. S10E). We posit that narrow pore size and distribution of the gel substrate will increase particle homogeneity, which, in turn, will enhance the efficacy of the nanosensor.

Gold nanoparticles demonstrate strong light scattering and absorption properties, resulting in the ability to distinguish regions populated by these nanoparticles and those that are depleted in them. Nanoparticle distribution in the gel nanosensor was visualized at two different depths (1 mm from the top and bottom each) in the gel using reflectance confocal microscopy (fig. S11A). Significant contrast between the hydrogel and gold nanoparticles was observed in the top 1-mm region of the gel nanosensor following exposure to 2 Gy. However, the bottom 1 mm shows a lower difference in contrast, likely indicating lower abundance of gold nanoparticles in this region of the gel nanosensor. These differences may be attributed to lower yields of gold nanoparticles at the bottom of the gel likely due to diffusional limitation of ascorbic acid (required for gold nanoparticle formation), which is only added to the top surface of the gel (fig. S11B). Note that the absorbance value at any location on the gel (used for dose predictions) is indicative of the ensemble average of nanoparticles present throughout the thickness at that location, because incident light traverses the entire depth of the gel. To that end, we observed no adverse impact of the nanoparticle distribution on the consistency, performance, and dose prediction efficacy of the gel nanosensor.

Skin cancer primarily near critical structures (eye) is usually treated by external beam radiation in light of potential complications with surgery and cosmetic considerations (39). To ensure that radiation is only delivered to the region of interest, radiation beams were shaped and contoured to maximize dose delivered to the target volume, while irradiation of nontarget healthy tissue is minimized. We therefore investigated the translational ability of the gel nanosensor for predicting topographical profiles of radiation delivered to a head and neck phantom (Fig. 4, A and B). An irregular crescent-shaped radiation dose field near the eye was delivered to the phantom to mimic clinically administered radiotherapy (Fig. 4, C and D). The distinct visual change in color is a qualitative indicator of the radiation delivered to the gel nanosensor (Fig. 4E). The dose profiles were predicted using the previously generated calibration (see Materials and Methods); the predicted absorbance dose is highest in the middle (bright red) of the pattern and decreases in intensity toward the edge (light red) of the field. Specifically, the core of the pattern receives an average dose of 2.3 Gy as designed by the treatment planning system, and the gel nanosensor predictions (average $\approx 2.3 \pm 0.26$ Gy) were in excellent agreement with the planned dose profile (Fig. 4, F and G, and fig. S12). These results demonstrate the ability of the gel nanosensor to detect and predict complex

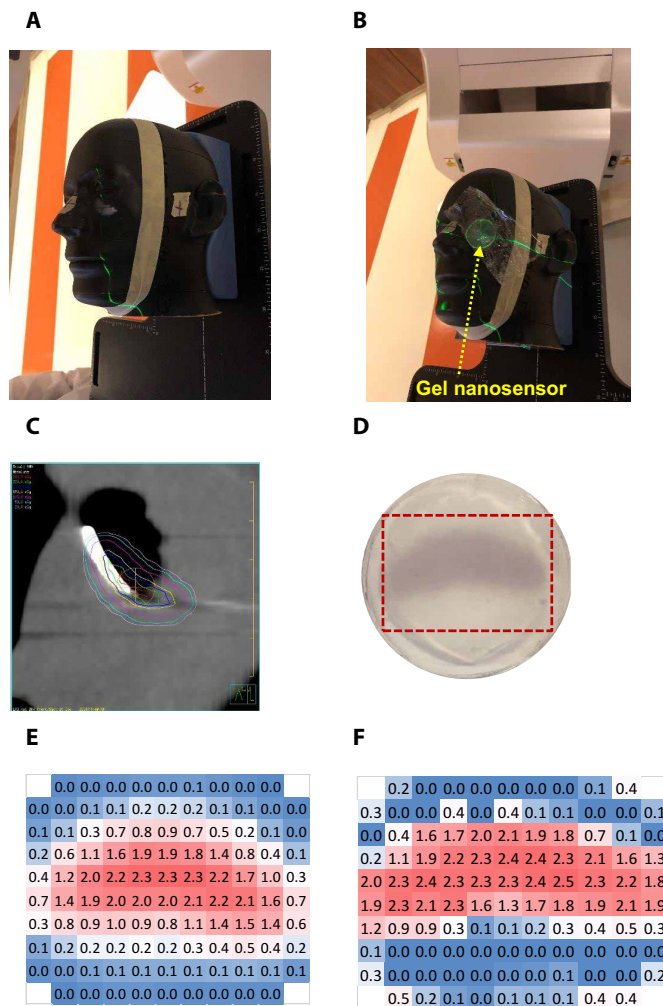


Fig. 4. Gel nanosensor enabled topographical detection and quantification of clinical radiation doses in anthropomorphic head and neck phantoms.

(A) Anthropomorphic head and neck phantom treated with an irregularly shaped x-ray radiation field below the left eye. (B) Image of the gel nanosensor positioned on the anthropomorphic phantom in the radiation field mimicking a conventional radiotherapy session. (C) Axial view of the treatment planning image along the central axis of the radiation beam representing an irregularly shaped radiation field used to deliver a complex radiation pattern under the eye of the phantom. The core of the crescent-shaped treatment region receives a radiation dose of 2.3 Gy (highlighted in red), and regions receiving lower doses are highlighted with different colors going outward (from green to light pink). (D) Visual image of the dose pattern on the gel nanosensor formed after delivery of 2.3 Gy. Only the irradiated region develops a maroon color, while the nonirradiated region remains colorless. (E) Expected topographical dose “heat map” profile of the radiation dose delivered to the gel placed in the phantom. The expected profile is generated from the treatment plan in the dose delivery system. In these figures, red and blue colors indicate higher and lower radiation doses, respectively. (F) Topographical doses predicted by the irradiated gel nanosensor. Absorbance values of ≈ 2 mm \times 2 mm grids were quantified using a calibration curve to generate the topographical dose profile. The anticipated dose received by the core of the crescent-shaped profile (2.3 Gy) is comparable to the dose profile predicted by the gel nanosensor (2.3 Gy), which demonstrates the capability of the gel nanosensor to qualitatively and quantitatively detect complex topographical dose profiles. The four independent experiments leading to these average values are shown in fig. S12. Photo credit: Sahil Inamdar, Arizona State University.

radiation patterns, including those used during actual clinical human radiotherapy.

Although mice and rats are widely used as model organisms and are inexpensive, their small anatomy relative to that of humans can lead to significant differences in dosimetry (40) and can limit the extrapolation of these findings to human patients. Canine patients circumvent these challenges because of their larger size, similarity in contours, and treatment methods to that of human patients. We investigated the efficacy of gel nanosensors as independent radiation dosimeters for verifying the dose delivered to two canine patients undergoing radiotherapy; the patients are henceforth referred to as “patient A” and “patient B.” The efficacy of the gel nanosensor was also compared with conventional radiochromic films used in the clinic. To our knowledge, this is the first time that a nanoscale dosimeter has been used in the detection of radiation dose delivered to live canine patients undergoing clinical treatments.

The surface of canine patient A was administered a dose of 2 Gy to the skin (Fig. 5 and fig. S13). The gel nanosensor was positioned at the edge of the radiation field, and the ability to measure topographical dose information was evaluated (Fig. 5 and fig. S13). Upon completion of the treatment, maroon color formation is seen on one-half of the gel; the nonirradiated region remained colorless (Fig. 5E). The previously generated calibration curve was used to predict the delivered dose. Unsurprisingly, the dose delivered is highest in the irradiated region (denoted by red squares). As expected, the intensity decreases from left to right (dark red to light red to blue), indicating a decrease in the intensity of the delivered radiation dose. Specifically, the predictions of the gel nanosensor of ≈ 2 Gy in the irradiated region were in excellent agreement with the treatment planning system (2-Gy planned dose) and the radiochromic film (≈ 2.1 Gy). The gel nanosensor also predicted that the region outside the irradiated region received minimal radiation (≈ 0.1 Gy), thereby illustrating its capability for predicting topographical dose profiles. The gel nanosensor predicts the irradiated and nonirradiated region effectively, and the performance is comparable to the predictions of a conventional radiochromic film (Fig. 5, E and F), which requires much longer wait times (>24 hours) for readout.

Canine patient B received a fractionated dose of 3 Gy at the target tumor site on the surface of skin (Fig. 6 and fig. S13) and 1.5 Gy on the surface above the bolus (fig. S13; see Materials and Methods for details). The tissue-equivalent bolus, made from synthetic vinyl polymer, is used to facilitate maximal and homogeneous dose deposition at the target site (skin in this case) (41). A visible change in color was observed over the entire gel, which was placed underneath the bolus (Fig. 6F). The gel nanosensor estimates a core uniform dose of ≈ 2.8 Gy, while the radiochromic film estimates a dose of ≈ 3.2 Gy. Predictions by both the gel nanosensor and the radiochromic film closely match the 3-Gy dose, which was planned using the delivery system. Note that the time required for color development and evaluation of the radiochromic film was >24 hours, which contrasts with that for the gel nanosensor that was only ~ 1 hour (color formation is visible in a matter of 10 min). In addition, it is possible to generate tissue-conformal formulations with the gel nanosensor, but this is difficult with the more rigid radiographic films. Further, Gafchromic films respond to low levels of nonspecific UV light (fig. S14A), but the gel nanosensor showed no such response, indicating its low propensity for false positives. In addition, the response of the gel nanosensor was maintained over the course of at least 7 days, indicating the potential for long-term retrieval of dosing data

(fig. S14B); this is a significant advantage over other polymer dosimeters that rely on fluorescence; the response is lost in a matter of minutes upon continuous readout (fig. S14C).

To visualize topographical dose profiles in a clinical radiotherapy setting, half of the gel nanosensor was placed on top of the bolus, which was placed on the skin of the canine patient B (Fig. 6); this half was exposed to a dose of 1.5 Gy as planned by the radiotherapy delivery system. As expected, the irradiated region turned maroon, while the nonirradiated area remained colorless (Fig. 6H). The gel nanosensor predicted a dose of ≈ 1.7 Gy in the core of the irradiated region, while the radiochromic film predicted a dose of ≈ 1.4 Gy. The gel nanosensor predicted that regions outside the irradiated path received no dose (predicted dose ≈ 0 Gy), which was consistent with the prediction of the radiochromic film. Together, the canine radiotherapy results indicate that the simplicity of fabrication, operation, readout time, and cost effectiveness ($\approx \$0.50$ cents per gel; only material cost was considered) demonstrates the translational potential of the colorimetric gel nanosensor for detecting and predicting topographical radiation doses in clinical radiotherapy.

CONCLUSIONS

To our knowledge, this is the first demonstration of a colorimetric gel nanosensor for detecting and distinguishing regions exposed to irradiation. The addition of a chemical quenching agent, sodium sulfide, reveals topographical dose distribution obtained during clinical radiotherapy. The effect of formulation conditions including gold salt and surfactant concentrations, gel pore sizes, and administration of the quenching agent were investigated to optimize the performance of the gel nanosensor. TEM indicated the formation of ≈ 50 -nm-diameter gold nanoparticles, and reflectance confocal microscopy was used to obtain information on nanoparticle distribution in the gel nanosensor. Controlling the pore size and distribution in the gel substrate will further enhance the efficacy of the nanosensor. Various simple and complex dose motifs were visualized using the gel nanosensor, which illustrates the ability of the sensor to capture dose profiles obtained in fractionated clinical radiotherapy. The effectiveness of the sensor was evaluated for predicting complex topographical dose profiles delivered to an anthropomorphic head and neck phantom and for visualizing and quantifying topographical dose distribution in live canine patients undergoing radiotherapy. The effectiveness of the gel nanosensor was comparable to the Gafchromic EBT3 films, which suffer from significant limitations. The ease of fabrication, simple operation procedures that require only a spectrophotometer, rapid and stable readout, possibility of formulating tissue-conformal geometries, and relatively low cost ($\approx \$0.50$ per gel nanosensor) indicate the highly disruptive and translational potential of the gel nanosensor technology for determining complex topographical dose distribution profiles in clinical radiotherapy, which will lead to improved patient safety and outcomes.

MATERIALS AND METHODS

Materials

Hydrogen tetrachloroaurate trihydrate ($\text{HAuCl}_4 \cdot 3\text{H}_2\text{O}$), myristyltrimethylammonium bromide (C_{14}TAB) (99%), L-ascorbic acid, sodium sulfide nonahydrate ($\text{Na}_2\text{S} \cdot 9\text{H}_2\text{O}$), sodium chloride, sodium bromide, sodium iodide, molecular biology-grade agarose, and 50-nm-diameter gold nanoparticles were acquired from Sigma-Aldrich. No further purification

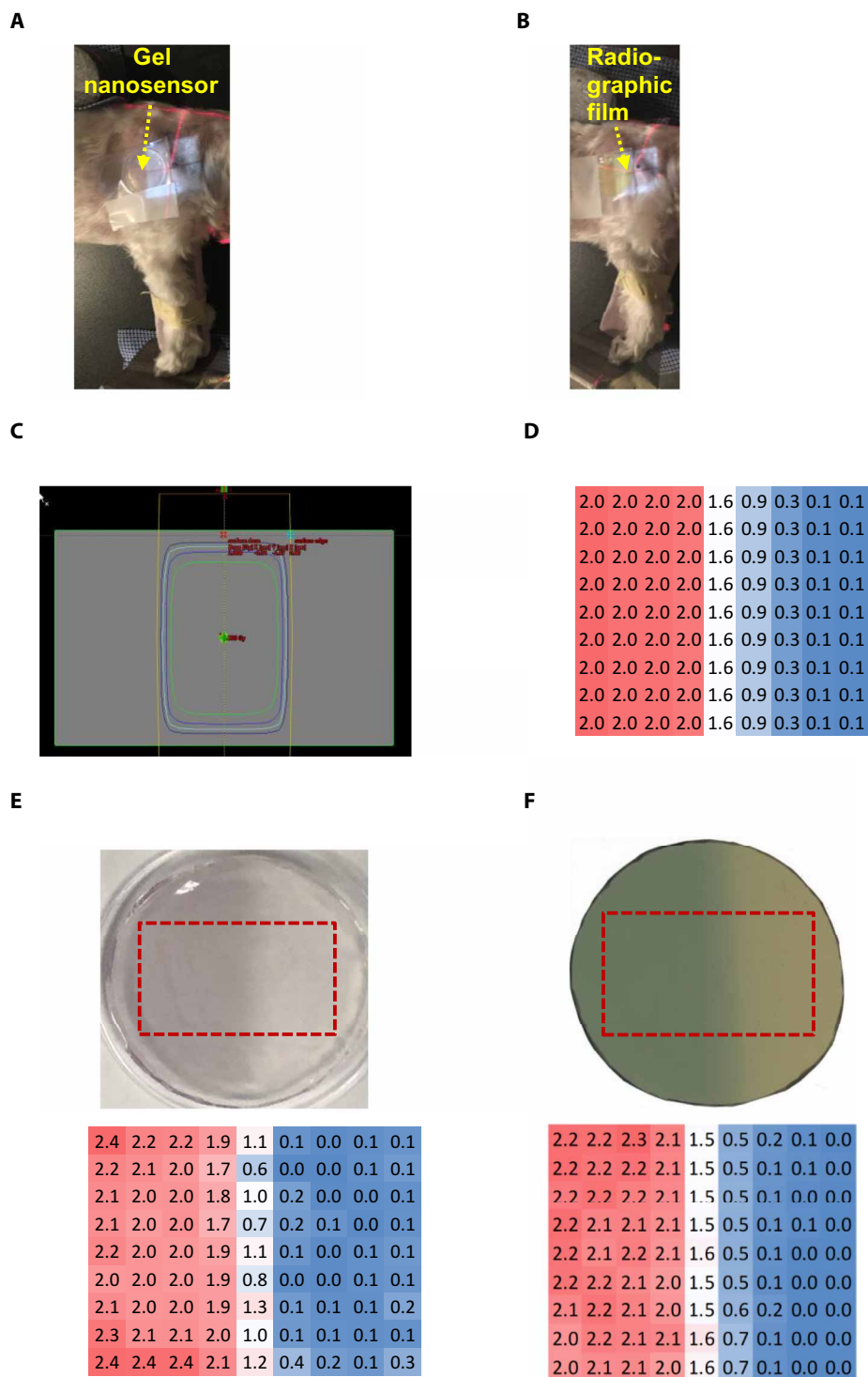


Fig. 5. Gel nanosensor enabled topographical detection and quantification of radiation delivered to canine patient A undergoing clinical radiotherapy. Representative image of (A) half of the gel nanosensor and (B) half of the radiographic film positioned in the radiation field delivered to canine patient A. (C) Treatment planning software depicting the delivery of a 2-Gy dose delivered to the surface of patient A (neon green edge along the rectangular gray box indicates the region receiving the 2-Gy dose). (D) The irradiated region received a dose of 2 Gy (highlighted in red squares), with irradiation dose dropping to a minimal radiation 0.1 Gy (highlighted in blue squares) outside the field of irradiation. A color change is visible in both the (E) gel nanosensor whose color changes to maroon and (F) radiographic film whose color changes to dark green after irradiation. The predicted dose map in the gel nanosensor (Na₂S addition wait time of 30 min and incubation time of 10 min) and radiographic film are shown below each corresponding sensor (see Materials and Methods for details). Similarity in the dose profiles indicates the efficacy of the gel nanosensor for clinical dosimetry. The time for readout of the gel nanosensor was 1 hour after irradiation, while the radiochromic film required >24 hours of developing time before readout. All experiments were carried out three independent times. Photo credit: Sahil Inamdar, Arizona State University.

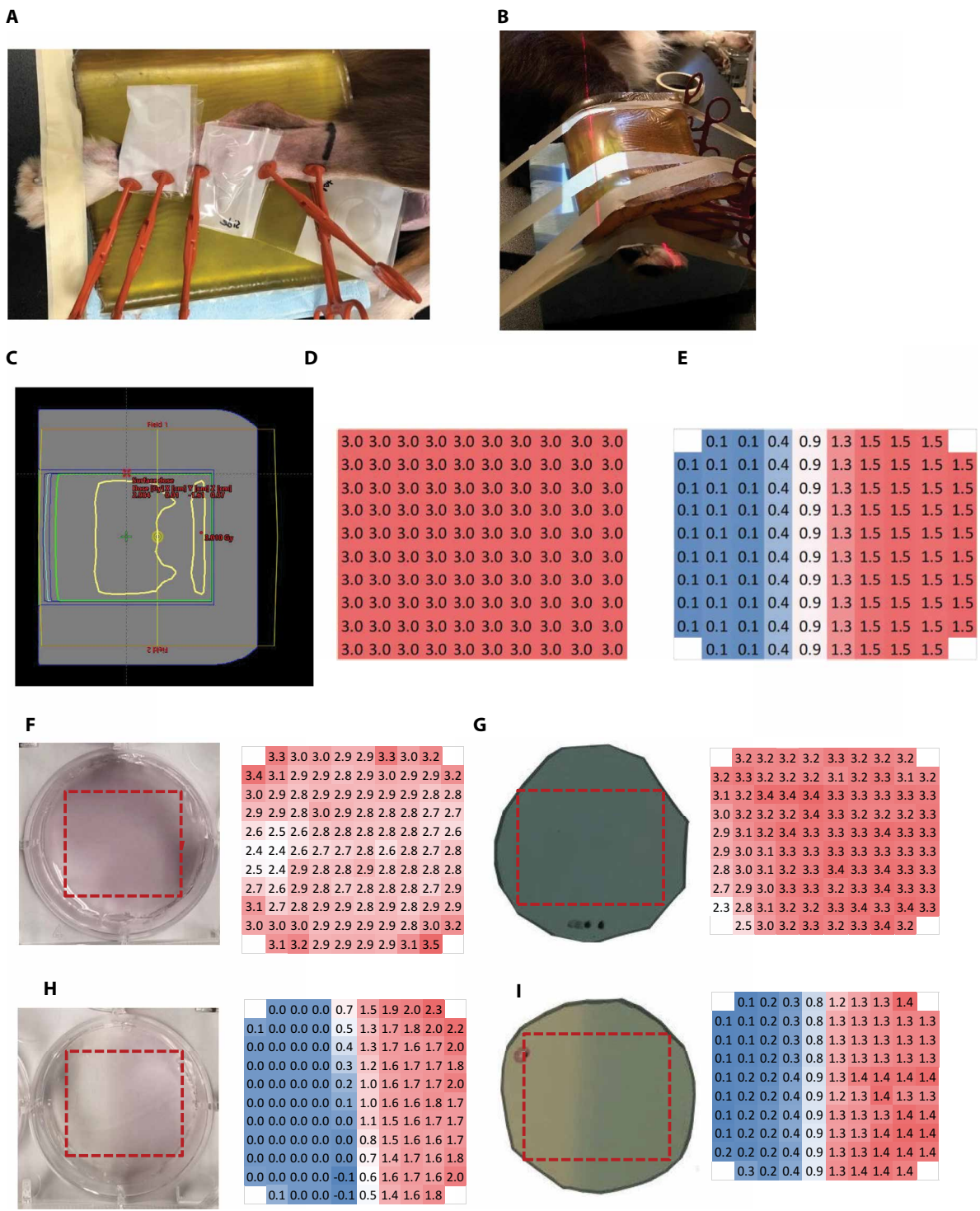


Fig. 6. Gel nanosensor enabled simultaneous detection and quantification of topographical and full-area doses delivered to canine patient B undergoing clinical radiotherapy. (A) Representative image of the gel nanosensor placed on the treated region, which was delivered a radiation dose of 3 Gy. (B) Representative image of the final setup of canine patient B. Half of the gel nanosensor and the Gafchromic EBT3 film is placed on the radiation field on top of the bolus, which was delivered a radiation dose of 1.5 Gy (image does not contain the gel nanosensor and the Gafchromic EBT3). (C) Treatment planning software depicting the delivery of a 3-Gy dose delivered to the skin of patient B (neon green edge indicates the region receiving the 3-Gy dose) (D) Expected dose delivered to the skin of the patient and (E) surface dose (1.5 cm above the bolus). A color change is easily visible in both the (F) gel nanosensor (maroon) and (G) radiographic film (dark green) after irradiation. The heat map of the predicted dose for both the gel nanosensor and radiographic film is depicted below each corresponding sensor (see Materials and Methods for details). The dose profiles are similar in all cases, indicating the efficacy of the gel nanosensor to clinical dosimetry. The time for readout of the gel nanosensor was 1 hour, while the radiochromic film required >24 hours before readout. All experiments were performed three times independently. Photo credit: Sahil Inamdar, Arizona State University.

of the chemicals was carried out. MilliQ water (18.2 megohm-cm) was used as solvent for all experiments conducted. Clear-bottom 96-, 24-, and 6-well plates, used as molds for the fabrication of the gel nanosensor, were purchased from Corning Incorporated.

Preparation of the precursor gel nanosensor

Tetrachloroauric acid (30 μ l of 1, 5, and 10 mM in MilliQ water) was mixed with C₁₄TAB surfactant (600 μ l of 50, 62.5, 75, 100, or 150 mM stock concentration in MilliQ water). From the resulting mixture, 100 μ l was discarded before further use. Agarose was dissolved in MilliQ water to obtain a final concentration of 2% (w/v) and heated until a clear transparent solution was obtained. This heated agarose (500 μ l) was added to the tetrachloroauric and cationic surfactant mixture. The above liquid (650 μ l) was poured into a 24-well tissue culture well plate to form the gel nanosensor with a thickness of \sim 3 mm and a diameter of \sim 1.5 cm. The final concentration of tetrachloroauric acid in the gel nanosensor is 0.025, 0.125, or 0.25 mM for the abovementioned stock concentrations, which ranged between 1 and 10 mM, and the final weight percentage of agarose is 1% (w/v). The final concentration of C₁₄TAB was calculated as 24.5, 31, 37, 49, and 73.5 mM for the abovementioned stock concentrations, which ranged between 50 and 150 mM. Ascorbic acid (650 μ l of 10 mM in MilliQ water) was allowed to diffuse from the top of the gel for 10 min, and excess ascorbic acid was discarded. The gel was washed using MilliQ water to further remove any excess ascorbic acid on the surface. Gel nanosensors were also prepared in six-well tissue culture plates (\approx 3.5 cm diameter) using similar procedures to investigate larger dimensions. Briefly, 82 μ l of 10 mM tetrachloroauric acid was mixed with 1.63 ml of 75 mM C₁₄TAB. From the resulting mixture, 272 μ l was discarded before further use. Heated liquid agarose [1.44 ml of 2% (w/v) in MilliQ water] was added to the above mixture and directly poured into a six-well tissue culture plate to form the gel nanosensor. The final concentration of tetrachloroauric acid in the gel nanosensor is \approx 0.25 mM, and the final weight percentage of agarose is 1% (w/v). The final concentration of C₁₄TAB was calculated as \approx 37 mM. For studies involving the effect of pore size distribution of the hydrogel on the radiation response of gel nanosensor, three additional weight percentages, 1.25, 0.75, and 0.4% (w/v), were used to fabricate the nanosensor.

Topographical dose visualization using gel nanosensors

All irradiation experiments were carried out at the Banner MD Anderson Cancer Center in Gilbert, AZ. A Varian TrueBeam linear accelerator was used to irradiate the samples with x-rays and energy of 6 MV at a dose rate of 600 monitor units (MU)/min (6 Gy/min). For complete exposure of the samples to irradiation, gel nanosensors were placed within a 10 cm \times 10 cm irradiation field. For studies on topographical dose distribution, only part (e.g., half) of the gel nanosensor was placed within the 10 cm \times 10 cm irradiation field, while the rest was placed outside the field. After irradiation, the samples were analyzed further at Arizona State University (ASU) in Tempe, AZ (travel time of approximately 30 min between the two institutions). Various quenching agents, Na₂S and NaX, where X = Cl, Br, or I (650 μ l of 5 mM), were investigated to arrest the nanoparticle formation reaction, resulting in restriction of gold nanoparticle formation to the irradiated region, which, in turn, facilitates topographical dose visualization. The quenching agents were added on top of the gel nanosensor 2, 5, 10, 20, or 30 min after irradiation (called “wait times”) and incubated for 10 min. The liquid on the

surface was discarded after incubation, and the gel nanosensors were analyzed further for dose quantification.

Dose quantification using absorbance spectroscopy

A BioTek Synergy 2 plate reader was used to quantify absorbance spectra of all samples for wavelengths ranging from 300 to 990 nm with a step size of 10 nm. Absorbance measurements for all samples were obtained 1 hour after irradiation, although the color formation was seen as early as 10 min. The absorbance value of MilliQ water at all wavelengths was used as the blank in all corresponding measurements. These values were then normalized by subtracting the absorbance value at a 990-nm wavelength for each gel nanosensor sample. The absorbance value at 540 nm was measured for all irradiated and non-irradiated gels and was offset by their corresponding absorbance value at 990 nm. These values were further corrected by subtracting the $A_{540\text{nm}} - A_{990\text{nm}}$ value obtained for MilliQ water. To ensure that the absorbance corresponding to the nonirradiated gel nanosensor (0 Gy) is 0, absorbance of the nonirradiated gel nanosensor (0 Gy) is subtracted from itself and the absorbance of the irradiated gel nanosensor. These values were plotted as a function of the radiation dose (in Gy, where 1 Gy = 1 J of energy absorbed/kg) to generate a calibration curve.

Transmission electron microscopy

Irradiated gels were dissolved in 1,2-propanediol (chaotropic agent) to facilitate drop casting onto TEM grids and heated to 80°C for 15 min. This mixture was centrifuged at 4000 rpm for 10 min. The supernatant was removed and was further dispersed in MilliQ water. This solution was further cast onto TEM grids. The samples were dried in air overnight and visualized using a CM200-FEG instrument operating at 200 kV in the LeRoy Eyring Center for Solid State Sciences at ASU. Elemental analysis was carried out to determine the composition of the nanoparticles formed. The diameter of nanoparticles formed was quantified by analyzing TEM images. Briefly, the perimeter of \sim 150 nanoparticles was individually measured using ImageJ software (U.S. National Institutes of Health, Bethesda, MD, USA; <https://imagej.nih.gov/ij/>; 1997–2018). This perimeter was divided by π to obtain the diameter of the nanoparticles assuming a circular geometry. In case of the 0-Gy condition, a total of \sim 100 nanoparticles were used because of the relative homogeneity observed in the nanoparticle population.

Quantification of number of nanoparticles formed

Gold nanoparticle standards with known dimensions (50 nm diameter) and concentration (3.5×10^{10} particles/ml) were used as standard for the estimation of the number of radiolytically generated gold nanoparticles in the gel nanosensor. Briefly, stock concentrations of gold nanoparticles with different particle numbers were prepared, and 100 μ l of the dispersion was pipetted into a 96-well plate. To this, 100 μ l of 2% (w/v) heated liquid agarose was added and mixed. The final particle number in each well plate ranges between 3.5×10^9 and 3.5×10^8 . Upon gelation of these hydrogels, the peak absorbance at 540 nm was measured and plotted as a function of number of gold nanoparticles to generate the calibration curve. The number of nanoparticles formed in radiation-treated gel nanosensors was determined using this standard calibration curve. Methods for determining the fractional conversion of gold ions to nanoparticles are provided in the Supplementary Materials.

Photostability study of fluorescein

Freshly prepared fluorescein solution (100 μ l of 0.2 mM in MilliQ water) was pipetted in a 96-well plate. Each well was exposed to a 400-nm wavelength laser with a spot size of 2 mm and a power of 180 mW for the corresponding time interval. After exposure to the laser, the fluorescence emission was measured at 515 nm. The loss in signal was normalized on the basis of the fluorescence emission of pristine fluorescein (not exposed to laser).

Reflectance confocal microscopy

A Leica TCS SP5 AOBS spectral confocal system was used to acquire images in the reflectance mode using a 40 \times water immersion lens to obtain information on the nanoparticle distribution within the gel. Z-stack images were acquired in slices of 10 μ m using an argon ion laser with a 488-nm wavelength. Each plane represents a 100 μ m \times 100 μ m field of view. Two-dimensional (2D) confocal Z stacks (\approx 100 slices) were stacked on ImageJ, and the 3D volume projection was obtained.

Topographical dose determination in an anthropomorphic head and neck phantom

An anthropomorphic head and neck phantom was used to determine the efficacy of topographical dose determination of the gel nanosensor in a clinical setting. Computer tomography (CT) images (1-mm slices) were acquired throughout the head region and transferred to a Philips Pinnacle treatment planning system. To simulate an actual clinical treatment, an irregularly shaped gross target volume (GTV) was generated using several CT images. The GTV was defined superficially above the left maxillary sinus, and a single 6-MV highly conformal photon (x-ray) beam was aimed at a discrete angle at the target to avoid nearby critical structures such as the left orbit. A multileaf collimator was used to shape and conform the radiation dose to a target field of 2.5 cm \times 1.9 cm. Within this target region, a crescent-shaped beam was delivered using the multileaf collimator. Radiation beams incident on contoured anatomical structures led to uncertainty and nonuniformity in the radiation dose deposited (42). To flatten the surface exposed to ionizing radiation and ensure homogeneous dose deposition, a 1.5-cm synthetic vinyl gel with physical properties similar to that of tissue (tissue equivalent “bolus”) was placed over the target area. In addition, the use of a bolus facilitates deposition of maximal dose on the skin surface based on dose deposition profiles in x-ray radiotherapy (43). In the absence of the bolus, the radiation dose deposited is typically less than the prescribed dose, which could potentially lead to suboptimal therapeutic outcomes (43). A single dose (2 Gy) was delivered to the surface of the head and neck phantom.

Topographical dose determination in canine cancer patients undergoing radiotherapy

Before the canine study, the experimental protocol described below was documented and approved by ASU’s Institutional Animal Care and Use Committee (IACUC). A consent form, approved by ASU’s IACUC, was signed by the pet owner before any study.

Irradiation of canine patients

Before irradiation, both canine patients, called A and B here, were anaesthetized to assist immobilization during treatment. Patient A’s skin received a radiation dose of 2 Gy within a field size of 4 cm \times

4 cm, and patient B’s skin received a radiation dose of 3 Gy within a field size of 6 cm \times 14 cm. To achieve maximum dose deposition and to enable a dose buildup to the skin (10), a 1.5-cm bolus was wrapped around the leg of patient B. The gel nanosensor (\approx 3.5 cm diameter) and a Gafchromic EBT3 film (\approx 3.5 cm diameter) were wrapped in a plastic bag to prevent direct contact with the skin of the patient. One-half of the gel nanosensor and the Gafchromic EBT3 film were placed on the region, which was exposed to radiation, while the other half of each was placed outside the field of irradiation. For patient A, the gel nanosensor and the Gafchromic EBT3 film were placed on the skin, while for patient B, they were placed on top of the bolus to demonstrate broader applicability. In addition, in the case of patient B, a separate gel nanosensor and Gafchromic EBT3 film were placed entirely within the radiation field underneath the bolus to validate the delivery of the 3-Gy dose to the skin surface. Following radiation treatment, the gel nanosensor and Gafchromic EBT3 films were removed and analyzed as described in the following sections.

Topographical mapping of Gafchromic EBT3 films

Following irradiation with x-rays, an EPSON Expression 10000XL Graphic Arts scanner was used to scan films before analysis, consistent with clinical practice (44). After scanning, the RIT dosimetry software (RIT113 Classic V6.0) was used to analyze digitized image of the films. Pixel values at discrete points with a 2-mm spacing between each point were measured along the digitized films. Each pixel value is correlated to the predicted dose using clinical standard calibration curve, and a corresponding topographical dose map is acquired. The regions receiving a high radiation dose are depicted in red, and those receiving a low irradiation dose are depicted in blue.

Topographical mapping of gel nanosensors

Absorbance values at 540 and 990 nm were determined along the surface of the entire gel (diameter of \approx 1.5 cm) using a 1536-well plate setup in a BioTek Synergy 2 plate reader. Each grid has a finite size of \approx 2 mm \times 2 mm, which results in approximately 110 grids along the entire gel for which the absorbance values are obtained, leading to a dose map on the gel surface. The final absorbance value at a given grid was calculated on the basis of the method described for generating the calibration curve. The calibration curve was used to predict the radiation dose delivered to each point on the grid, and a corresponding topographical dose map over the entire gel surface is obtained. The regions that received high doses of radiation are depicted in red, and those receiving low radiation doses are depicted in blue.

Image acquisition

All optical images of the gel nanosensor were acquired using an Apple iPhone 7 or a Samsung Galaxy S8 camera under ambient lighting and automatic settings, which were maintained throughout the course of the study. The images were cropped to the desired size for representation. No further editing or post-processing was carried out. These images were not used for quantification of the dose but only for visualization of the gels.

Statistical analyses

All irradiation experiments were carried out a minimum of three times independently unless otherwise mentioned. The average and

SD were calculated using the average and stdev functions in Microsoft Excel for Office 365 MSO. The results are expressed as average \pm 1 SD. Statistical significance was calculated using Student's *t* test using a two-tailed distribution with the function *t.test* on Microsoft Excel for Office 365 MSO. In all cases, *P* values of <0.05 are considered statistically significant.

SUPPLEMENTARY MATERIALS

Supplementary material for this article is available at <http://advances.sciencemag.org/cgi/content/full/5/11/eaaw8704/DC1>

Fig. S1. Schematic illustration of the proposed mechanism for the formation of gold nanoparticles upon irradiation with ionizing radiation.

Fig. S2. Plot of peak absorbance at 540 nm versus radiation dose shows the gel nanosensor response as a function of C₁₄TAB concentration and a fixed wait time of 5 min for Na₂S addition in all cases.

Fig. S3. Images of gel nanosensors, fabricated in 24-well plates and containing 37 mM C₁₄TAB, irradiated with different radiation doses (0 to 10 Gy).

Fig. S4. Effect of wait time before Na₂S addition on gel nanosensor response.

Fig. S5. Effect of wait time before Na₂S addition following irradiation on gel nanosensor response.

Fig. S6. Schematic illustration of the proposed mechanism used for detecting spatial dose distribution.

Fig. S7. Effect of gold salt concentration on the gel nanosensor response and estimation of precursor gold ion conversion to gold nanoparticles.

Fig. S8. Gel nanosensor fabricated in six-well plates (\approx 3.5 cm diameter and same thickness as before, i.e., \approx 3 mm) with 37 mM C₁₄TAB and 0.25 mM gold salt was carried out before evaluation as a sensor for the detection of therapeutically relevant radiation doses.

Fig. S9. Elemental analyses of nanoparticles.

Fig. S10. Response of the gel nanosensor to varying agarose pore size distribution was evaluated by modulating the weight percentage of agarose used during fabrication.

Fig. S11. Confocal reflectance microscopy imaging of the gel nanosensor and images depicting ascorbic acid diffusion along the depth of the gel nanosensor.

Fig. S12. Four independent experiments showing topographical radiation dose profiles for the gel nanosensor in a head and neck phantom; the average values of these four independent data are presented in Fig. 4.

Fig. S13. Schematic illustration of the canine patient set up for topographical dosimetry and visualization using gel nanosensors.

Fig. S14. Evaluation of photostability, photobleaching, and long-term storage response of the gel nanosensors.

Reference (45)

REFERENCES AND NOTES

- M. J. Zelefsky, J. O. Deasy, Improved long-term outcomes with IMRT: Is it better technology or better physics? *Int. J. Radiat. Oncol. Biol. Phys.* **87**, 867–868 (2013).
- P. G. S. Prasanna, H. B. Stone, R. S. Wong, J. Capala, E. J. Bernhard, B. Vikram, C. N. Coleman, Normal tissue protection for improving radiotherapy: Where are the Gaps? *Transl. Cancer Res.* **1**, 35–48 (2012).
- S. T. Lutz, J. Jones, E. Chow, Role of radiation therapy in palliative care of the patient with cancer. *J. Clin. Oncol.* **32**, 2913–2919 (2014).
- G. Huang, G. Medlam, J. Lee, S. Billingsley, J.-P. Bissonnette, J. Ringash, G. Kane, D. C. Hodgson, Error in the delivery of radiation therapy: Results of a quality assurance review. *Int. J. Radiat. Oncol. Biol. Phys.* **61**, 1590–1595 (2005).
- G. A. Patton, D. K. Gaffney, J. H. Moeller, Facilitation of radiotherapeutic error by computerized record and verify systems. *Int. J. Radiat. Oncol. Biol. Phys.* **56**, 50–57 (2003).
- P. Zyganski, C. Abkai, Z. Han, Y. Shulevich, D. Menicelli, J. Hesser, Low-cost flexible thin-film detector for medical dosimetry applications. *J. Appl. Clin. Med. Phys.* **15**, 311–326 (2014).
- S. F. Kry, S. A. Smith, R. Weathers, M. Stovall, Skin dose during radiotherapy: A summary and general estimation technique. *J. Appl. Clin. Med. Phys.* **13**, –3734 (2012).
- R. Ravichandran, J. P. Binukumar, I. A. Amri, C. A. Davis, Diamond detector in absorbed dose measurements in high-energy linear accelerator photon and electron beams. *J. Appl. Clin. Med. Phys.* **17**, 291–303 (2016).
- S. Devic, N. Tomic, D. Lewis, Reference radiochromic film dosimetry: Review of technical aspects. *Phys. Med.* **32**, 541–556 (2016).
- M. M. Eyadeh, M. Wierzbicki, K. R. Diamond, Measurement of skin surface dose distributions in radiation therapy using poly(vinyl alcohol) cryogel dosimeters. *J. Appl. Clin. Med. Phys.* **18**, 153–162 (2017).
- R. Dreindl, D. Georg, M. Stock, Radiochromic film dosimetry: Considerations on precision and accuracy for EBT2 and EBT3 type films. *Z. Med. Phys.* **24**, 153–163 (2014).
- K. Pushpavanam, E. Narayanan, K. Rege, Molecular and nanoscale sensors for detecting ionizing radiation in radiotherapy. *ChemNanoMat* **2**, 385–395 (2016).
- M.-E. Lecavalier, M. Goulet, C. N. Allen, L. Beaulieu, D. Larivière, Water-dispersible colloidal quantum dots for the detection of ionizing radiation. *Chem. Commun.* **49**, 11629–11631 (2013).
- F. P. Doty, C. A. Bauer, A. J. Skulan, P. G. Grant, M. D. Allendorf, Scintillating metal-organic frameworks: A new class of radiation detection materials. *Adv. Mater.* **21**, 95–101 (2008).
- S. M. Abtahi, Characteristics of a novel polymer gel dosimeter formula for MRI scanning: Dosimetry, toxicity and temporal stability of response. *Phys. Med.* **32**, 1156–1161 (2016).
- J. M. Warman, M. P. de Haas, L. H. Luthjens, L. H. P. Murrer, A radio-fluorogenic organic gel for real-time, 3D radiation dosimetry. *Adv. Mater.* **23**, 4953–4955 (2011).
- K. Saha, S. S. Agasti, C. Kim, X. Li, V. M. Rotello, Gold nanoparticles in chemical and biological sensing. *Chem. Rev.* **112**, 2739–2779 (2012).
- H.-C. Huang, S. Barua, G. Sharma, S. K. Dey, K. Rege, Inorganic nanoparticles for cancer imaging and therapy. *J. Control. Release* **155**, 344–357 (2011).
- R. Urie, D. Ghosh, I. Ridha, K. Rege, Inorganic nanomaterials for soft tissue repair and regeneration. *Annu. Rev. Biomed. Eng.* **20**, 353–374 (2018).
- K. Pushpavanam, E. Narayanan, J. Chang, S. Sapareto, K. Rege, A colorimetric plasmonic nanosensor for dosimetry of therapeutic levels of ionizing radiation. *ACS Nano* **9**, 11540–11550 (2015).
- S. Inamdar, K. Pushpavanam, J. M. Lentz, M. Bues, A. Anand, K. Rege, Hydrogel nanosensors for colorimetric detection and dosimetry in proton beam radiotherapy. *ACS Appl. Mater. Interfaces* **10**, 3274–3281 (2018).
- K. Pushpavanam, S. Inamdar, J. Chang, T. Bista, S. Sapareto, K. Rege, Detection of therapeutic levels of ionizing radiation using plasmonic nanosensor gels. *Adv. Funct. Mater.* **27**, 1606724 (2017).
- S. Anandhakumar, R. Rajaram, J. Mathiyarasu, Unusual seedless approach to gold nanoparticle synthesis: Application to selective rapid naked eye detection of mercury(II). *Analyst* **139**, 3356–3359 (2014).
- J. W. T. Spinks, R. J. Woods, *An Introduction to Radiation Chemistry* (Wiley, 1990).
- Z. Khan, T. Singh, J. I. Hussain, A. A. Hashmi, Au(III)–CTAB reduction by ascorbic acid: Preparation and characterization of gold nanoparticles. *Colloids Surf. B. Biointerfaces* **104**, 11–17 (2013).
- H. Akisada, J. Kuwahara, A. Koga, H. Motoyama, H. Kaneda, Unusual behavior of CMC for binary mixtures of alkyltrimethylammonium bromides: Dependence on chain length difference. *J. Colloid Interface Sci.* **315**, 678–684 (2007).
- Y. Takenaka, Y. Kawabata, H. Kitahata, M. Yoshida, Y. Matsuzawa, T. Ohzono, Effects of surfactant concentration on formation of high-aspect-ratio gold nanorods. *J. Colloid Interface Sci.* **407**, 265–272 (2013).
- J. Pérez-Juste, L. M. Liz-Marzán, S. Carnie, D. Y. C. Chan, P. Mulvaney, Electric-field-directed growth of gold nanorods in aqueous surfactant solutions. *Adv. Funct. Mater.* **14**, 571–579 (2004).
- J. Polte, Fundamental growth principles of colloidal metal nanoparticles—A new perspective. *CrystEngComm* **17**, 6809–6830 (2015).
- N. Pernodet, M. Maaloum, B. Tinland, Pore size of agarose gels by atomic force microscopy. *Electrophoresis* **18**, 55–58 (1997).
- J. A. Edgar, A. M. McDonagh, M. B. Cortie, Formation of gold nanorods by a stochastic “popcorn” mechanism. *ACS Nano* **6**, 1116–1125 (2012).
- T. Morris, H. Copeland, G. Szulczewski, Synthesis and characterization of gold sulfide nanoparticles. *Langmuir* **18**, 535–539 (2002).
- P. H. Charles, G. Cranmer-Sargison, D. I. Thwaites, S. B. Crowe, T. Kairn, R. T. Knight, J. Kenny, C. M. Langton, J. V. Trapp, A practical and theoretical definition of very small field size for radiotherapy output factor measurements. *Med. Phys.* **41**, 041707 (2014).
- J.-P. Pignol, B. M. Keller, A. Ravi, Doses to internal organs for various breast radiation techniques—Implications on the risk of secondary cancers and cardiomyopathy. *Radiat. Oncol.* **6**, 5 (2011).
- R. M. Shymko, D. L. Hauser, J. O. Archambeau, Field size dependence of radiation sensitivity and dose fractionation response in skin. *Int. J. Radiat. Oncol. Biol. Phys.* **11**, 1143–1148 (1985).
- J. A. Bearden, X-ray wavelengths. *Rev. Mod. Phys.* **39**, 78–124 (1967).
- N. C. Stellwagen, Electrophoresis of DNA in agarose gels, polyacrylamide gels and in free solution. *Electrophoresis* **30** (suppl. 1), S188–S195 (2009).
- M. M. Chui, R. J. Phillips, M. J. McCarthy, Measurement of the porous microstructure of hydrogels by nuclear magnetic resonance. *J. Colloid Interface Sci.* **174**, 336–344 (1995).
- K. Reddy, T. Strom, C. Chen, Primary radiotherapy for locally advanced skin cancer near the eye. *Pract. Radiat. Oncol.* **2**, 63–72 (2012).
- L. Padilla, C. Lee, R. Milner, A. Shahlaee, W. E. Bolch, Canine anatomic phantom for preclinical dosimetry in internal emitter therapy. *J. Nucl. Med.* **49**, 446–452 (2008).

41. V. Vyas, L. Palmer, R. Mudge, R. Jiang, A. Fleck, B. Schaly, E. Osei, P. Charland, On bolus for megavoltage photon and electron radiation therapy. *Med. Dosim.* **38**, 268–273 (2013).
42. M. Łukowiak, K. Jezierska, M. Boehlke, M. Więcko, A. Łukowiak, W. Podraza, M. Lewocki, B. Masojć, M. Falco, Utilization of a 3D printer to fabricate boluses used for electron therapy of skin lesions of the eye canthi. *J. Appl. Clin. Med. Phys.* **18**, 76–81 (2017).
43. F. M. Khan, *The Physics of Radiation Therapy* (Lippincott Williams & Wilkins, 2010).
44. N. Tagiling, R. Ab Rashid, S. N. A. Azhan, N. Dollah, M. Geso, W. N. Rahman, Effect of scanning parameters on dose-response of radiochromic films irradiated with photon and electron beams. *Heliyon* **4**, e00864 (2018).
45. L.-f. Zhang, C.-y. Zhang, Controlled growth of concave gold nanobars with high surface-enhanced Raman-scattering and excellent catalytic activities. *Nanoscale* **5**, 5794–5800 (2013).

Acknowledgments: We thank R. Nityanandan for help with reflectance confocal microscopy and for analyzing the distribution of gold nanoparticles in the gel nanosensor. We are grateful to J. Kilbourne (Department of Animal Care Technologies, ASU) for invaluable help with the IACUC protocol for these studies and for several helpful discussions. K.R., K.P., and S.S. are authors on a patent application related to this work filed by Arizona State University and Banner Health (patent application number US201662275168P, published on 27 July 2017).

Funding: We acknowledge the National Science Foundation (NSF-CBET 1403860) for funding this research. **Author contributions:** K.P. and K.R. conceived and executed the development of the gel nanosensor for topographical dose mapping. K.P., S.D., and S.I. carried out the experiments in the study including data analysis. T.B., T.S., and S.S. set up and executed all gel irradiation protocols including the head and neck phantom studies. E.B. set up and executed the canine radiotherapy protocols. K.P. and K.R. wrote the manuscript. All authors have agreed on the final version of the manuscript. **Competing interests:** The authors declare that they have no competing interests. **Data and materials availability:** All data needed to evaluate the conclusions in the paper are present in the paper and/or the Supplementary Materials. Additional data related to this paper may be requested from the authors.

Submitted 31 January 2019

Accepted 20 September 2019

Published 15 November 2019

10.1126/sciadv.aaw8704

Citation: K. Pushpavanam, S. Inamdar, S. Dutta, T. Bista, T. Sokolowski, E. Boshoven, S. Sapareto, K. Rege, Determination of topographical radiation dose profiles using gel nanosensors. *Sci. Adv.* **5**, eaaw8704 (2019).